

# Small Antenna Testing in a Compact Antenna Test Range

S.F. Gregson<sup>1,2</sup>

<sup>1</sup>Next Phase Measurements  
11521 Monarch St, Garden Grove, CA,  
USA  
stuart.gregson@npmeas.com

C.G. Parini<sup>2</sup>

<sup>2</sup>School of Electronic Engineering and  
Computer Science  
Queen Mary University of London  
London, UK

S. Pivnenko<sup>3</sup>

<sup>3</sup>Antenna Systems Solutions  
C/ Albert Einstein, 14  
Santander, 39011, Cantabria, Spain

**Abstract**—The Compact Antenna Test Range (CATR) was initially conceived as an efficient way of testing electrically large antennas at very much reduced, fixed, range lengths than would otherwise be the case. However, when testing lower gain, physically smaller antennas, the measurements can become susceptible to inhomogeneities within the CATR QZ including phenomena associated with edge diffraction effects, feed spill-over, chamber multipath *etc.* Whilst it has been demonstrated experimentally that many of these measurement artefacts may be effectively mitigated using standard and modern more sophisticated post-processing techniques. This paper supports those findings through simulation of the direct and indirect far field ranges and by careful examination of the data processing chain. Results are presented, the relative success of the various techniques examined and the utility of this is set, and expounded, in the context of modern, *i.e.* 5G, communications systems.

## I. INTRODUCTION

Direct far-field (DFF) testing has become the de facto standard for sub GHz over the air (OTA) testing of the physical layer of radio access networks when using orthogonal frequency division multiplexing (OFDM) type waveforms [1]. However, when using the DFF method, the antenna under test (AUT) should be separated from the remote source antenna by a distance that is proportional to the frequency and proportional to the square of the maximum dimension of the AUT [2]. This suggests that when using the DFF method at mm-wave frequencies, as is the case for 5G new radio (5G NR), for all but the smallest of antennas, indoor screened test systems become impractically large. Compact antenna test ranges (CATR) were originally conceived as an indirect far-field (IFF) method for testing electrically large antennas at fixed range lengths that are very much smaller than that which would otherwise be the case. Thus of late, and largely as a consequence of this attribute CATRs have found great utility in many > 6 GHz 5G NR test applications with the 3<sup>rd</sup> Generation Partnership Project (3GPP) recently designating the CATR based IFF method as being the *only* test solution suitable for all three antenna classifications [1].

Complex 5G NR multiple input multiple output (MIMO) active antenna systems (AAS) require careful calibration of the amplitude and phase between respective RF paths within the device. This is typically required to equalize electrical path lengths and to ensure that the active electronics are not being driven into compression. We need a robust way to calibrate the Massive MIMO antenna array without requiring an excessive amount of channel state information (CSI) feedback which would otherwise be the case. An additional part of the

calibration process involves the antenna pattern measurement which is often influenced by mutual coupling within the AAS [3]. However, in contrast to the communication system level testing, these measurements can be performed utilizing conventional continuous wave signals. Low gain, small antennas, such as those contained within the AAS tend to sample the CATR pseudo plane wave across a comparatively small volume of space making their measurement susceptible to the influence of the high spatial frequency amplitude and phase ripple in the quiet zone [4]. Thus, a view has to some extent formed that, the measurement of small, low gain, antennas in a CATR is best avoided. Placing the test antenna at the centre of the measurement coordinate system minimizes the translation experienced during the measurement thereby preserving the local uniformity of the illuminating field and, as is illustrated below, is ultimately only of very limited assistance. However, this strategy is not practical, or possible, when testing an element within an AAS where many of the individual antennas will very likely be displaced quite significantly. However, if the electrically small test antenna is displaced then it affords the opportunity to use more modern sophisticated mode-based filtering techniques to correct the measurements, *e.g.* Mathematical Absorber Reflection Suppression [2]. Whilst one could potentially use traditional strategies such as complex averaging [2] or Advanced Antenna Pattern Correction [2, 4] here however, we can take advantage of the inherent displacement within the measurement and avoid the need for repeat measurements where enormous care needs to be taken to translate the AUT by a known, very carefully controlled amount. This paper presents the results of this study and culminates with a discussion of the effectiveness and optimisation of the technique highlighting the relative merits of the approaches treaded herein.

## II. OVERVIEW OF DFF MEASUREMENT SIMULATION

The reaction theorem is a widely used method for analysing coupling problems [2, 4, 6]. This theorem shows that, provided the electric and magnetic field vectors ( $\underline{E}_1, \underline{H}_1$ ) and ( $\underline{E}_2, \underline{H}_2$ ) are known, of the same frequency and monochromatic; then the mutual impedance,  $Z_{21}$ , between two radiators, say antenna 1 and 2, in the linear, homogeneous environment described by  $\epsilon, \mu$  may be expressed in terms of a surface integral [4, 6],

$$Z_{21} = \frac{V_{21}}{I_{11}} = -\frac{1}{I_{11}I_{22}} \int_{S_2} (\underline{E}_2 \times \underline{H}_1 - \underline{E}_1 \times \underline{H}_2) \cdot \underline{\hat{n}} ds \quad (1)$$

Here,  $\underline{\hat{n}}$  is taken to denote the outward pointing unit surface normal. The subscript 1 denotes parameters associated with

antenna 1 whilst the subscript 2 denotes quantities associated with antenna 2, *e.g.*  $S_2$  is an arbitrary but fixed closed surface that circumscribes antenna 2 but not antenna 1. Here,  $I_{11}$  is the current at the terminal of antenna 1 when it transmits and similarly,  $I_{22}$  is the equivalent for antenna 2 when it transmits. Crucially, amplitude *and* phase information are contained within the mutual impedance, which is clearly related to the coupling,  $S_{21}$ , between two antennas. Thus, as the mutual impedance and hence the coupling product will be a function of the displacement, their relative orientations and their respective polarization properties.

The use of this method can be illustrated by considering first, the DFF method. We may represent the Massive MIMO antenna, or a range of other radiators for that matter, in a very general way by considering them as being formed from an array of dipoles [7]. Thus, we may use a linear superposition of,

$$\underline{E}(r) = \frac{1}{\epsilon_0} \left\{ 2 \left( \frac{1}{\epsilon r^2} - \frac{jk_0}{\sqrt{\epsilon r}} \right) (\underline{p}_0 \cdot \hat{r}) \hat{r} + \left( \frac{1}{\epsilon r^2} - \frac{jk_0}{\sqrt{\epsilon r}} - k_0^2 \right) [\hat{r} \times (\hat{r} \times \underline{p}_0)] \right\} g(r, \omega) \quad (2)$$

and,

$$\underline{H}(r) = j\omega \left( \frac{1}{r} - jk_0 \sqrt{\epsilon} \right) (\hat{r} \times \underline{p}_0) g(r, \omega) \quad (3)$$

to compute the total radiated electric and magnetic near- or far-fields for a range of radiating structures. Here,  $g(r, \omega)$  denotes the free space Green function and assumes a negative, suppressed, time dependency which we must take into account. If we compute the coupling between this and a spherical wave of various radii, or field radiated by a known “remote” source antenna, we will obtain the measured field at a point in space. In the following examples, we fix the probe antenna at the desired distance  $D$  at 26 GHz and then physically rotate the AUT to determine the “measured” radiation pattern over a range of angles thereby building up the conventional far-field “measured” pattern.

Figure 1 shows the resulting “measured” radiation pattern of the array when illuminated by the remote source antenna (RSA) at a range of FF distances of  $1/10 R_{FF}$ ,  $1/4 R_{FF}$ ,  $1/3 R_{FF}$ ,  $1/2 R_{FF}$ ,  $R_{FF}$ ,  $2 R_{FF}$  where  $R_{FF}$  is the far-field distance as determined using the conventional Rayleigh far-field criteria [1, 2, 6] and where we have suppressed the  $1/R^2$  term from all of the plots so the shape of the radiation pattern and gain loss can be determined, *cf.* [6]. At 26 GHz the FF distance for the array is a little over seven meters and it is clear that apart from the  $0.1 R_{FF}$  case the general shape of the AUT pattern can be determined. Furthermore, the peak of the pattern varies by less than 0.25 dB between the maximum range length and the  $0.33 R_{FF}$  case.

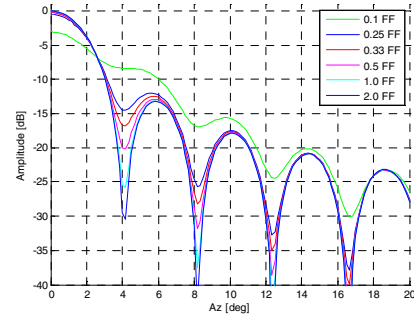


Figure 1. Antenna pattern of Massive MIMO antenna over a range of radii to illustrate the change in pattern with distance.

Looking now at the near-in side-lobes for all the range distances, shows that apart from the 0.1 FF case, all show the location of the side-lobe peak and null positions to relatively good accuracy. However, the null depth for the 0.25 FF case is very small for the first side-lobe (less than 3 dB) and so this is poorly defined and, since for MIMO applications null location and depth are important parameters, this range length would likely be problematic. However, the 0.33 FF and 0.5 FF cases clearly offer a good “measured” pattern performance at reduced range length. For the 0.33 FF case the null depth is shown to be 4 dB. Thus, if the tolerance on the gain and the null depth of the Massive MIMO antenna can be relaxed then it may be possible to also relax the range length requirements placed upon the far-field radius. Furthermore, this data can be used with the OTA communications system modelling presented in [6] to establish whether reducing the range length is feasible in a given application. Crucially, it has been found that in many applications the far-field distance requirement may be reduced by a significant factor without impacting the results of measurements of Error Vector Magnitude (EVM), Symbol Error Rate (SER), data throughput *etc.* The next sections show how this very general simulation method can be extended to consider measurements taken using the IFF method as opposed to the DFF method treated here.

### III. OVERVIEW OF IFF MEASUREMENT SIMULATION AND MM-WAVE MASSIVE MIMO ARRAY CALIBRATION

Equation (1) can be used to evaluate the pattern measured by an arbitrary but known CATR [4] the fields illuminating the AUT from the CATR only needs to be computed once per frequency. This is also true for the fields radiated by the AUT however their evaluation, using for example the method presented in Section 1 above, is far less computationally intensive. Details of the simulation of the fields propagated to the CATR quiet zone (QZ) can be found in the open literature, *e.g.* [4]. Thus, it is possible to examine the impact of various properties of the CATR, *e.g.* amplitude taper, amplitude ripple, phase ripple and range reflections, [2, 4] by constructing one or more pseudo plane wave(s) of our choosing. Thus, the electric and magnetic fields of a perfect  $x$ -polarised plane wave propagating in the positive  $z$ -direction can be expressed using,

$$\underline{E}(x, y, z) = A(x, y) e^{-jk_0 z} \hat{e}_x \quad (4)$$

Here, we have assumed a positive, suppressed, time dependency,  $A$  denotes the complex wave amplitude and  $k_0$  the free-space propagation constant. Thus, we may create a plane

wave with amplitude taper, amplitude ripple and phase ripple of our choosing using, for example [4],

$$A(x, y) = \sin\left(\frac{n_x \pi x}{L_x}\right) \sin\left(\frac{n_y \pi y}{L_y}\right) \quad (5)$$

Here,  $n_x, n_y$  denotes the number of ripples in the  $x$ - and  $y$ -axes respectively and  $L_x, L_y$  denote the width of the CATR QZ in the  $x$ - and  $y$ -axes. Similar expressions can be used to perturb the phase function. The corresponding magnetic fields can be obtained from the TEM condition. Thus, using the fields we have constructed, together with the AUT fields and equation (1) we can compute the “measured” antenna pattern for this AUT CATR combination. In this way we may examine the effect various CATR QZ properties have on our measurements. In this example we see that the ripple corresponds to producing an error that is largely located around a narrow angular range. Furthermore, from inspection of Figures 2 – 5 we see that the higher the spatial frequency the wider out the effect on the resulting far-field pattern appears. Thus, this angle is closely related to the spatial frequency of the amplitude QZ ripple with this link not previously having been reported in these terms. Although the peak-to-peak amplitude of the ripple is typically specified and subsequently verified as part of the implementation of a CATR, the spatial frequency and spectral content of that parameter is generally not considered. Thus, depending upon the application, this may perhaps be an oversight.

The impact that various CATR QZ properties have on the ensuing antenna measurements is considered more fully in [8, 9]. However, and as well as illustrating the utility and flexibility of the simulation technique considered here, it is clear from the results of these simulations that the quality and properties of the CATR QZ are inextricably and intimately related to the measurement errors encountered when using these systems. Thus, understanding the detailed properties of the QZ is crucial if the CATR is to be used successfully. This is further illustrated by consideration of the calibration of the Massive MIMO antenna.

Standard MIMO networks tend to use two or four antennas to transmit data and two or four antennas to receive it. Conversely, Massive MIMO systems have an especially large number of transmitting antennas. These systems increase the number of Tx antennas to typically many hundreds at a base station. Massive MIMO apply amplitude and phase changes to signal to form a beam and this is implemented, largely, by means of a pre-code which is incorporated into to the signal. Conceptually however, this corresponds to the arrangement illustrated in Figure 6. Thus, correction of individual RF paths through the AAS due to variances in T/R modules, beam-forming network, manufacturing and assembly tolerances becomes highly desirable [10, 11, 12]. Additionally, during production there is also a requirement to perform a functionality test to ensure that there is no compression of the amplifiers as this introduces spectral regrowth. Thus, the calibration can't be completed entirely within the AAS and instead must be performed OTA as mutual coupling within the array must also be taken account with the large number of elements making conductive testing impractical. Calibration of the Massive MIMO antenna can be accomplished by means of several techniques [10, 11, 12] with a commonly utilised technique involving illuminating the AAS with a plane-wave and recording the response through each individual RF path. However, if this illumination is provided by the CATR pseudo plane-wave, then the relative transmission amplitude and phase will be correspondingly modulated by inhomogeneities within the pseudo plane wave. Thus, the accuracy and precision of the calibration of the array will be critically dependent upon the quality of the CATR QZ.

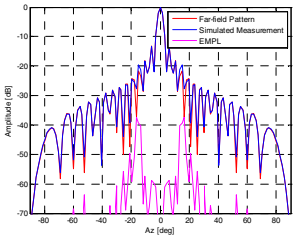


Figure 2. 10 Amplitude ripples across QZ

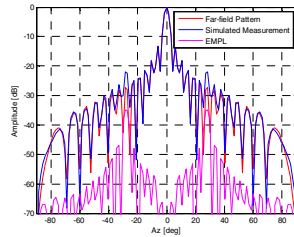


Figure 3. 20 Amplitude ripples across QZ

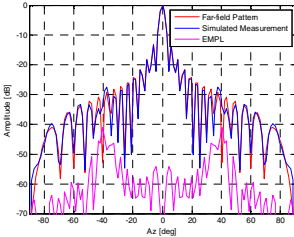


Figure 4. 30 Amplitude ripples across QZ

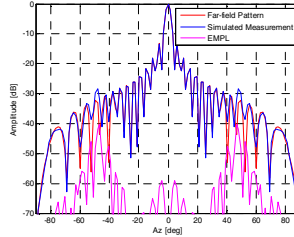


Figure 5. 40 Amplitude ripples across QZ

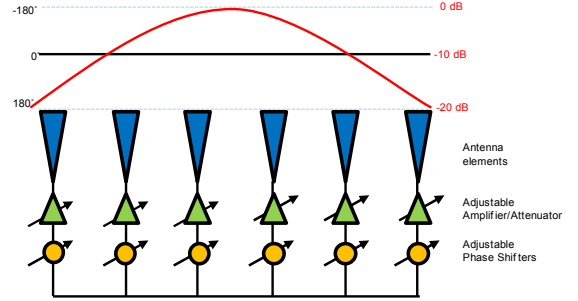


Figure 6. Illustration of Active Array System

Although the array as a whole can be shown to behave as a spatially extended aperture antenna which tends to average out the small localised fluctuations within the pseudo plane wave; conversely, when testing the individual RF paths and their corresponding elements, these electrically small antennas generally sample the QZ field at a localised point in space. To illustrate the effect that this has on a typical 5G mm-wave Massive MIMO antenna, the coupled amplitude and phase at each element in a typical mm-wave 5G array antenna was computed and can be seen presented in Figures 7 and 8 respectively. The coupling was calculated across 400 MHz bandwidth for each element within the array when the array way located centrally within the CATR QZ. This is denoted by the red trace.

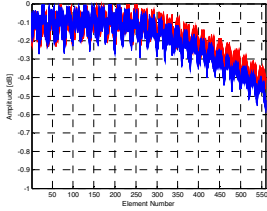


Figure 7. 30 Amplitude ripples across QZ

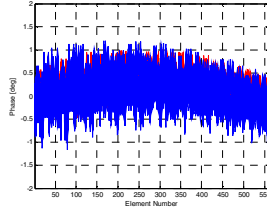


Figure 8. 40 Amplitude ripples across QZ

From inspection, it is evident that this is a rapidly varying, fairly pathological, function in both space & frequency. The coupling is clearly affected by both the amplitude taper (slowly varying taper) and the ripple (rapidly varying ripple). This calculation was repeated for the case of an array displaced by  $1 \lambda$  in  $x$  and  $1 \lambda$  in  $y$  (blue) to assess the sensitivity of this result to the positioning of the AAS. For a given element the variation in measured amplitude across the frequency band is 0.25 dB and across the complete array was shown to be 0.45 dB. Here, the taper impacts on Gain, EIRP, TRP, *etc.* and the ripple on the calibration of the individual guided wave paths. Thus, successful calibration of an AAS relies upon a very well behaved CATR QZ. As the taper is highly dependent upon feed pattern, with the ripple being largely dependent upon reflector edge treatment and illumination this behaviour is a function of frequency with broader frequency bands tending to increase the variation experienced. Calibration is possible if we have a well-designed CATR, however this can only be achieved to within a finite limit. Even for the case where we use a comparison measurement against some absolute truth model, *e.g.* a golden antenna where we must ensure that the installation of the antennas can be performed in a manner that is very highly reproduceable, as the correction is a rapidly fluctuating quantity. The next section examines the pattern measurement of low gain antennas in a CATR since, and as we have begun to explore here, these place very special demands on the test system that require further examination.

#### IV. PATTERN CORRECTION OF LOW GAIN ANTENNAS MEASUREMENTS ON A CATR

As expounded above, the measurement of low gain antennas can prove difficult when using CATRs. Although initially conceived as a means for testing electrically large antennas there are many instances that call for the use of a CATR to measure electrically smaller, low gain, antennas. However, mode filtering based post-processing techniques have been successfully deployed to correct many forms of antenna measurements including those made using CATRs [2, 13]. Although CATRs require that the AUT be kept within the volume of the QZ for the duration of the measurement, these translational, mode orthogonalisation, based post-processing techniques are particularly well suited to the measurement of low gain antennas where the more modest physical size of the radiator means that the requisite translation does not render the measurement infeasible. This section uses the modelling method developed above to examine the effectiveness of this strategy before progressing to compare the results against alternative, more traditional strategies [2]. Thus, equation (1) was used to simulation several CATR measurements where several spurious interfering sources were introduced into the measurement simulation in order to perturb the resulting

“measured” far-field pattern. These were respectively: Single interferer located at  $60^\circ$  at -20 dB, dual interferers at  $60^\circ$  at -20 dB and  $-45^\circ$  at -25 dB, triple interferers at  $60^\circ$  at -20 dB,  $-45^\circ$  at -25 dB and  $20^\circ$  at -30 dB and extreme case of quadruple interferers at  $60^\circ$  at -20 dB,  $-45^\circ$  @ -25 dB,  $20^\circ$  at -30 dB and  $-90^\circ$  at -5 dB. As will be presented, this last case was also examined using alternative, less sophisticated, more traditional, correction techniques.

The far-field pattern was processed by translating the AUT to the origin of the measurement coordinate system. The equivalent cylindrical mode expansion could then be obtained using standard cylindrical near-field theory [2], filtered to remove the influence of the perturbing scatterer whereupon the resulting processed far-field could be obtained. A detailed treatment of this technique is presented in the open literature, *e.g.* [2, 8, 11]. Figures 9, 11, 13 and 15 contain the CMC plots for the four cases defined above. Here, the red trace denotes the equivalent CMC spectra prior to filtering with the blue trace representing the band-pass filtered spectrum. Figures 10, 12, 14 and 16 present the equivalent far-field patterns for these four test cases. Here, the red trace denotes the reference ideal far-field pattern that can be used as the absolute “truth” model. The black trace is the perturbed far-field “measurement”, the blue trace is the mode filtered, processed result with the magenta trace representing the dB difference level between the ideal and processed patterns [2]. The RMS difference level for each case was also computed prior to and following the MARS processing to illustrate the degree of agreement attained as well as to provide a measure of the improvement achieved. Here, for the first time, additional interferers were introduced in order to allow the careful examination of the ability of the technique to mitigate measurement artefacts in more complicated clutter environments.

From inspection of the far-field patterns it is clear that in all four cases, the degree of clutter rejection achieved is very encouraging. Table 1 presents a summary of the RMS difference levels which we may use as an additional quantitative measure of adjacency [2]. In each case we have achieved an improvement of between 12 dB and more than 20 dB. The limited improvement obtained in Case 1 is a result of the comparatively close agreement from which we were starting. Conversely, Case 4 constituted a particularly demanding case where one of the four interferers was placed at  $90^\circ$  and only 5 dB below the pseudo plane wave itself.

In addition to the four test cases described above, a fifth case was considered which employed the conventional strategy of locating the AUT precisely at the origin of the measurement coordinate system thereby insuring the AUT occupied as small a portion of the CATR QZ as was possible. Here, the MARS processing can be seen to be ineffective, this is expected. Also, the resulting pattern is smooth, which is a result of the minimum phase difference between the direct and interfering signals and the corresponding absence of rapid constructive and destructive interference. However, as is clear from the traces and the high -11 dB RMS difference level, the resulting “measured” amplitude is inaccurate. One further “traditional” strategy that can be deployed is to take repeat acquisitions having displaced the AUT by a small amount. The far-field phase function is corrected for the translation and the complex

average of the measurements is used as an improved estimate of the true pattern. In this case, the results were grossly inaccurate, *i.e.* unusable, so instead a related but slightly more sophisticated approach was taken. The Advanced Antenna Pattern Correction (AAPC) technique requires the acquisition of three, or preferably more patterns, each having been displaced by a small but precisely known amount and then fitting this phase corrected data to a circle in the complex Argand plane [2, 14].

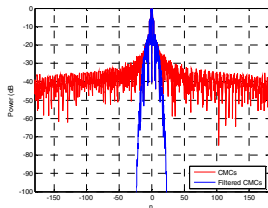


Figure 9. CMCs –  $\times 1$  interfering signal

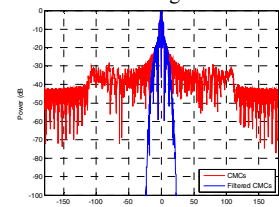


Figure 11. CMCs –  $\times 2$  interfering signal

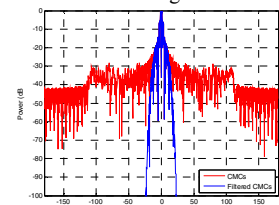


Figure 13. CMCs –  $\times 3$  interfering signal

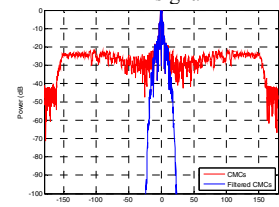


Figure 15. CMCs –  $\times 4$  interfering signal

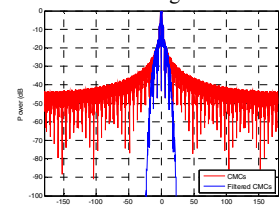


Figure 17. CMCs –  $\times 4$  interfering signal – conventional measurement

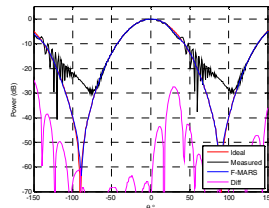


Figure 10. FF Pattern,  $\times 1$  interfering signal

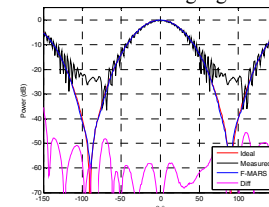


Figure 12. FF Pattern,  $\times 2$  interfering signal

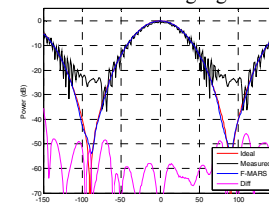


Figure 14. FF Pattern,  $\times 3$  interfering signal

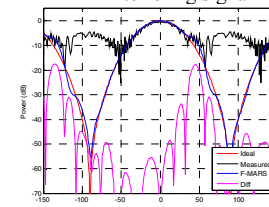


Figure 16. FF Pattern,  $\times 4$  interfering signal

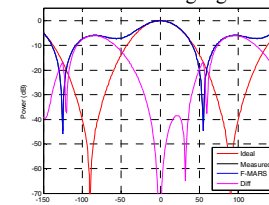


Figure 18. FF Pattern,  $\times 4$  interfering signal – conventional measurement

respectively. This is a very encouraging result as the technique had been able to recover the pattern nulls around  $\pm 90^\circ$  that were, without the processing, almost entirely obscured by the interference.

TABLE I. SUMMARY OF RMS DIFFERENCE LEVELS.

Test Case	RMS Difference Before Correction	RMS Difference After Correction	Improvement in RMS dB
1	-27.2	-39.0	11.8
2	-26.4	-50.8	24.4
3	-25.9	-50.7	24.8
4	-10.5	-28.8	18.3
5	-11.3	NA	0.0
6	-11.3	-21.0	9.7
7	-11.3	-24.1	12.8

Clearly, both the three-point and four-point implementations of the AAPC method work to some extent for this very demanding test case. However, it is quite clear from these figures and Table 1, that the four-point implementation worked better, although each exhibit localised discontinuities where the function fit has effectively failed resulting in spikes appearing in the patterns that are clearly erroneous. Thus, although the MARS processing provided a slightly improved result, *cf.* Case 4, which exhibited an RMS difference level that was better than Case 7 by *circa* 3 dB this does not convey the full story as the sharp discontinuities in the AAPC result require additional processing, *e.g.* the application of a boxcar median average filter function, or the acquisition of even more pattern cuts.

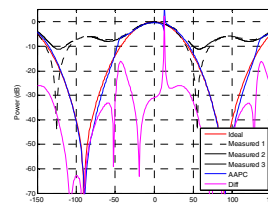


Figure 19.  $\times 3$  Pattern cuts, *cf.* Case 6 of Table 1.

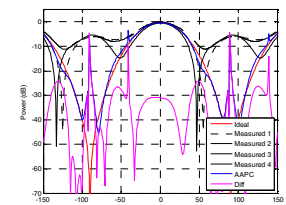


Figure 20.  $\times 4$  Pattern cuts, *cf.* Case 7 of Table 1.

All of the techniques considered require the measurement of phase data. However, from a practical perspective the AAPC method requires the AUT to be displaced very carefully and precisely in the  $x$ - and  $z$ -axes which can become challenging and would normally require the use of additional precision positioning equipment. Although the mode filtering technique also requires the AUT to be displaced, the exact amount and way in which the AUT is translated is not critical and, importantly, only a *single* pattern cut is required.

## V. EXAMINATION OF SUITABILITY OF VARIOUS MODE FILTERING WINDOWING FUNCTIONS

Figure 19 presents the results for the case where three cuts were used whereas Figure 20 presents the results of the case where the circle was fitted to four points with the RMS difference levels being summarised in Table 1 as Cases 6 and 7

The last topic that was investigated as part of this study was the choice of windowing function that is used to apply the band pass filter to the cylindrical mode coefficients (CMC). As the algorithm depends upon a Fourier transform to convert

between mode and angular domains, it is sensible to examine the effect that the various potential windowing functions have on the harmonic signals as we are operating in the presence of both broad-band noise and nearby strong harmonic interference. Typically, rectangular, spherical MARS or cosine functions have been used in the various implementations of this mode filtering algorithm. However, a comparative examination of the relative merits of these filter functions in the context of the CMC based processing has not been considered in any great detail. Here, several different filter functions were selected from the myriad that are available, *cf.* [15]. Case 1 of Table II was the rectangular, brick-wall filter function. This was used in the early development of the CMC based filtering technique, but quickly abandoned thereafter. The relatively poor result shown in Table II reinforces this position. Case 2 of Table II utilised the filter function that is routinely used with the spherical mode-based algorithm [8]. However, as can be seen this was clearly not the optimum choice for the cylindrical case and as such other coefficients were used with the value of 0.9 being found to outperform the initial 1/2 value [16] that is more commonly used, this was Case 3. Another widely used function is the cosine and cosine squared functions. These were examined and comprise Cases 4 and 5 respectively. Higher power functions were also tested with minimal differences being observed. The cosine squared function has the attractive property that both the function and its first derivative tend to zero at the boundaries. This is usually beneficial as one generally tries to match the function and as many of its higher order derivatives to zero as possible at the extremities so as to minimise spectral leakage [15].

TABLE II. SUMMARY OF RMS DIFFERENCE LEVELS FOR VARIOUS CYLINDRICAL MODE FILTERING FUNCTIONS.

Case	CMC Window function	Improvement in RMS dB
1.	Rectangular	4.5
2.	$0.5^{(n-NAUT_{max})}$	13.0
3.	$0.9^{(n-NAUT_{max})}$	22.2
4.	Cosine	25.9
5.	Cosine squared	27.7

This is clearly not an exhaustive survey and hence although this has confirmed that the cosine squared function is a very reasonable choice, the planned future work is to include examining the use of other windowing functions.

## VI. SUMMARY & CONCLUSION

This paper has presented the results of a recent modelling campaign that shows that low gain antennas can be measured accurately and precisely in a CATR providing enough care and effort are invested. This had been verified experimentally previously, *cf.* [13], however here, using computational simulation the success of the measurement and mode orthogonalization & filtering technique could be quantified, and the processing further optimised. The price of this very significant improvement in performance is the measurement of

phase, the displacement of the radiator, and the use of a highly efficient fast Fourier Transform (FFT) based post-processing routine and adherence to standard cylindrical sampling theory [2], none of which are particularly onerous. In addition to having been shown to have superior performance to more traditional approaches, this strategy is seen to be significantly less demanding in terms of experimental setup, data acquisition and time on range.

## REFERENCES

- [1] 3GPP, "TR 37.842 v13.2.0 TSG RAN E-UTRA and UTRA; Radio Frequency (RF) requirement background for Active Antenna System (AAS) Base Station (BS)," 2017.
- [2] C.G. Parini, S.F. Gregson, J. McCormick, D. Janse van Rensburg "Theory and Practice of Modern Antenna Range Measurements", IET Press, 2014, ISBN 978-1-84919-560-7.
- [3] B.L. Diamond, "A Generalized Approach to The Analysis of Infinite Planar Array Antennas", Proceedings of the IEEE, Volume: 56, Issue 11, Nov. 1968.
- [4] C.G. Parini, R. Dubrovka, S.F. Gregson, "Computational Electromagnetic Modelling of Compact Antenna Test Range Quiet Zone Probing: A Comparison of Simulation Techniques", EuCAP, Davos, 2016.
- [5] J. van Norel, A.H. van Gastel, V.J. Vokurka, J. Neve, J.F. Coroller, "Application of flexible scanning in advanced APC-techniques", AMTA 16<sup>th</sup> Annual Meeting & Symposium, Long Beach, California; October 1994.
- [6] S.F. Gregson, C.G. Parini, "Use of OTA System Performance Metrics in the Design & Optimization of CATRs for 5G Testing", AMTA Symposium and Meeting, San Diego, October 2019.
- [7] H.C. Chen, "Theory of Electromagnetic Waves, A Co-ordinate-Free Approach", McGraw-Hill, International Student Editions in Related Fields, 1985, ISBN 0-07-010688-6.
- [8] S.F. Gregson, C.G. Parini, A.C. Newell, P.N. Betjes, "Using Mathematical Absorber Reflection Suppression (Mars) To Partially Correct for The Non-Uniformity of A CATR Quiet Zone", ESA Workshop on Antenna Measurements, ESA ESTEC, October 2017.
- [9] S.F. Gregson, C.G. Parini, "Examination of the Effect of Common CATR Quiet Zone Specifications on Antenna Pattern Measurement Uncertainties", Loughborough Conference on Antennas and Propagation, Loughborough, November 2017.
- [10] R. Gogalin, O. Y. Bursalioglu, H. Papadopoulos, G. Caire, A. F. Molish, A. Michaloliakos, V. Balan, K. Psounis, "Scalable synchronizaiton and reciprocity calibration for distributed multiuser MIMO", IEEE Trans. Wireless Commun., vol. 13, no. 4, Apr 2014.
- [11] F. Kaltenberger, H. Jiang, M. Guillaud, R. Knapp, "Relative channel reciprocity calibration in MIMO/TDD systems", Proc. Future Network and mobile summit, 2010.
- [12] "Calibration procedure for TDD beam—forming", 3GPP RAN1 #51bis Sevilla Spain January 2008.
- [13] S.F. Gregson, J. Dupuy, C.G. Parini, A.C. Newell, G.E. Hindman, "Application of Mathematical Absorber Reflection Suppression to Far-Field Antenna Testing", LAPC, Loughborough, November 2011.
- [14] J. van Norel, A.H. van Gastel, V.J. Vokurka, J. Neve, J.F. Coroller, "Application of Flexible Scanning in Advanced APC-Techniques", AMTA 16<sup>th</sup> Annual Meeting & Symposium, October 1994.
- [15] F.J. Harris, "On the Use of Windows for Harmonic Analysis with the Discrete Fourier Transform", Proc. IEEE, Vol. 66, No. 1, January 1978, pp. 51 – 83.
- [16] S.F. Gregson, A.C. Newell, P.N. Betjes, C.G. Parini, "Verification of Spherical Mathematical Absorber Reflection Suppression in a Combination Spherical Near-Field and Compact Antenna Test Range", AMTA Symposium and Meeting, Atlanta, October 2017.